

Bernal Stacking and Symmetry-Inequivalent Antiferromagnetism in MSi_2N_4 Heterobilayers

Brandon Pedroza-Rojas^{1,2,*}, David W. Facemyer^{1,*} and Ariadna Sánchez-Castillo³

¹Department of Physics and Astronomy and Nanoscale and Quantum Phenomena Institute, Ohio University, Athens, Ohio 45701, USA

²Institute of Basic Sciences and Engineering, Autonomous University of the State of Hidalgo, Mineral de la Reforma, Hidalgo 42184, Mexico

³Superior School of Apan, Autonomous University of the State of Hidalgo, Chimalpa Tlalayote, Hidalgo 43920, Mexico

* These authors contributed equally to this work.

E-mail: bp297224@ohio.edu, pe484939@uaeh.edu.mx

E-mail: df008219@ohio.edu

E-mail: ariadna_sanchez@uaeh.edu.mx

Keywords: Van der Waals heterostructures, Antiferromagnetic spintronics, MA_2Z_4 family, Bernal stacking, Non-trivial Exchange interactions

Abstract

Layered MA_2Z_4 compounds, structural relatives of MoS_2 discovered in 2020, exhibit rich magnetic behavior arising from reduced dimensionality, noncentrosymmetric lattice symmetries, and stacking-dependent exchange interactions. Here, we investigate Bernal-like stackings in H-phase MA_2Z_4 ($\text{M} = \text{Mn}$ and Fe ; $\text{A} = \text{Si}$; $\text{Z} = \text{N}$) monolayers and bilayers by combining first-principles spin-dependent relaxation energies with a localized-spin Heisenberg description. From density-functional calculations, we extract the dominant intralayer exchange couplings up to third-nearest neighbors and the leading interlayer exchanges up to second-nearest neighbors, enabling construction of an effective bilayer spin Hamiltonian. We first analyze interface-driven proximity effects within a ferromagnetic reference configuration, demonstrating how recovery of AB-type stacking and spin alignment—while varying only the transition-metal species—provides a route for selectively tuning magnetic order and symmetry breaking within the $\text{P}6\text{m}2$ space group. Building on this microscopic understanding of the bonding environment, we then examine antiferromagnetic ordering tendencies in the coupled layers. Exact diagonalization of the resulting bilayer Hamiltonian reveals the magnetic ground state and low-lying excitation spectrum, showing that the interlayer exchange is not merely perturbative but competes directly with intralayer interactions in stabilizing the observed spin configurations. These results establish Bernal-stacked MA_2Z_4 bilayers as a platform in which stacking geometry and exchange hierarchy jointly govern magnetic reconstruction, offering a controlled pathway toward domain selection and spin-texture engineering in low-dimensional van der Waals materials.

1 Introduction

Van der Waals heterostructures (vdWHs) serve as essential frameworks for vertical-engineering in spintronic devices [1, 2], integrating magneto-resistive junctions to optimize quantum phenomena [3]. Recent advances in spin-orbit torque and magnonics have demonstrated room-temperature antiferromagnetic (AFM) tunneling junctions that circumvent ferromagnetic limitations, such as

incomplete polarization and field sensitivity [4–7]. These enable field-driven polarization with tunable magnetoresistance across antiparallel, parallel, and spin-inclination transitions [8, 9], complementing AFM spintronic paradigms [10, 11]. AFM insulators further harness thermal gradients for spin-current generation via the spin Seebeck effect [12].

Current demands for faster, durable electronics with sub-particle control [13] drive exploration of AFM semiconductors hosting coherent magnon-exciton interactions [14, 15], magnon-driven skyrmions [16], interfacial AFM skyrmions [17], and magnon-phonon coupling [18–20]. These phenomena emerge from collinear (Néel/stripe) or non-collinear orders [21], stabilized by spin-orbit coupling (SOC) [22]. Although graphene displays defect-enhanced magnetism [23, 24], silicon-based spintronics exhibits suboptimal performance [25]. This underperformance persists due to fundamental exchange-correlation phenomena that govern total spin magnetic moments [26–28].

The MA_2Z_4 family hosts a remarkably broad range of electronic and magnetic behaviors. Schottky barriers in these compounds enable efficient quantum tunneling [29], MoSi_2N_4 supports half-metallicity and valley polarization [30]. Their vdWHs further allow giant tunnel magnetoresistance [31] and strain-tunable Schottky responses [32]. Janus variants [33, 34], nanoribbons [34–38], and valleytronic applications [39–41] expand this landscape, often tied to their nontrivial topological phases [42]. Heavy-electrode configurations show high optical absorption [43], while MnSi_2N_4 (MSN) and FeSi_2N_4 (FSN) exhibit metallicity in the ferromagnetic (FM) order [44], pronounced optical activity [45], and sizable strain-tunable magnetic anisotropy (MAE = -345 peV/Mn) [46].

Regardless, the stripe-type AFM breaks the in-plane rotational symmetry inherent to the hexagonal lattice [47], promoting local distortion, end-chain defects, which enhances spin polarization [48] and supports time-reversal symmetry breaking [49]. Crucially, SOC stabilizes two-dimensional magnetism despite Mermin–Wagner constraints [50] by inducing magnetocrystalline anisotropy [51].

Using density functional theory (DFT) in the DFT-D3(BJ)+ U + J formulation, we characterize the monolayer-bilayer progression and identify the stripe-AFM ground state, along with its associated magnetic phase transitions. The extracted exchange landscape shows that the interlayer terms are not simply perturbative: the nearest-interlayer exchange is comparable to the dominant intralayer scale in one layer, while the next-nearest interlayer term competes directly with the weaker intralayer couplings in the other. To clarify the magnetic ordering tendencies that emerge from this hierarchy, we constructed a localized-spin model and examined its low-lying magnetic excitation spectrum through exact diagonalization. The resulting picture demonstrates how these competing exchange channels can stabilize intrinsic spin control across the two layers, enabling spin-valve-like configurations and functional FM/AFM tunnel-junction behavior in this class of bilayers (BLs).

2 Procedural Framework

A systematic investigation was conducted into the electronic and magnetic properties of these heterostructures. To this end, DFT+ U was employed, with the implementation being carried out using QUANTUM ESPRESSO 7.3.1 [52, 53]. The valence electron configurations for the projector augmented wave (PAW) pseudopotentials [54, 55] were defined as: Mn ($3s^23p^63d^54s^2$; 15 e^-), Fe ($3s^23p^63d^64s^2$; 16 e^-), Si ($3s^23p^2$; 4 e^-), and N ($2s^22p^3$; 5 e^-).

Scalar relativistic calculations were performed within the Local Spin Density Approximation (LSDA) for structural relaxations and collinear magnetic searching. For the calculations pertaining to the magnetocrystalline anisotropy (MAE), we incorporated spin-orbit coupling (SOC). A critical aspect of this methodology is the treatment of on-site Coulomb interactions. The Dudarev formulation [56], has proven to be a reliable tool for analyzing isotropic properties. However, its application is often hindered by the utilization of spherically averaged interactions, which can obscure more nuanced orbital-dependent effects. In addressing the preservation of anisotropic contributions to energy and the mitigation of suppression of orbital moments in the non-collinear regime, the rotationally invariant formulation proposed by Liechtenstein et al. [57] was employed.

Additionally, the accurate modeling of the interlayer binding in vdWHs necessitates a meticulous treatment of dispersion forces. The Grimme D3 correction was incorporated with Becke–Johnson (BJ) damping [58, 59]. The BJ damping scheme is meticulously designed to effectively attenuate the dispersion correction at short ranges, thereby preventing the unphysical double-counting of correlation effects already captured by the exchange-correlation functional. Concurrently, it ensures the accurate recovery of the long-range London dispersion behavior essential for 2D stacking trends.

3 Computational details

Spin-polarized Density Functional Theory (known as LSDA) calculations were performed using the Quantum Espresso package (QE) [52, 53]. Electron-ion interactions were described using the Projector Augmented Waves (PAW) pseudopotential method [54, 55], as in the first MA_2Z_4 , where it was shown by the authors to best match the experimental band gap results in MoSi_2N_4 . Additionally, exchange-correlation interactions were implemented using the Generalized Gradient Approximation (GGA) with the Perdew–Burke–Ernzerhof (PBE) parametrization [60].

For the treatment of van der Waals dispersions, the D3 semiempirical approach [58, 59, 61, 62], with Becke–Johnson damping correction [63], was employed. To describe the behavior of d -electrons, the Hubbard model was used [64, 65], of the Dudarev type, with $U_{\text{eff}} = U - J_0$, where values of 4.6/0.6 and 6.0/0.5 eV were used for the Hubbard and Hund components in Mn/Fe, respectively, as reported [66].

Electronic states were expanded using plane waves up to nearly 320 Ry and 600 Ry for the kinetic energy cutoff and the charge density cutoff, respectively, using a convergence test sequence for each monolayer, as shown in Tables 1. A convergence criterion of 1×10^{-8} Ry/Bohr was employed, with Fermi–Dirac smearing up to 0.01 Ry. To mitigate image interactions, vacuum layers of 30 and 50 Å were added in the z -direction for monolayers and bilayers, respectively.

The Brillouin zone was sampled using a Monkhorst–Pack grid [67]. LSDA was implemented in collinear mode and with spin–orbit coupling. Collinear calculations enabled the determination of the magnetic ground state for each magnetic monolayer and stacking configuration, as shown in Table 1.

Table 1: Initial collinear magnetization parameters: layered AFM and FM alignments in magnetic monolayers, and each stacking through minimum energy interlayer distances.

System	M_{atom}	E_{cut}^k (Ry)	E_{cut}^{ρ} (Ry)	k
A1-type AFM				
	$M_{Mn} = \pm 1$	120	480	$5 \times 5 \times 1$
A2-type AFM				
	$M_{Fe} = \pm 1$	145	580	$7 \times 7 \times 1$
A3-type AFM				
FM	$M_{Mn} = +1, M_{Fe} = +1$	80	320	$7 \times 7 \times 1$
BLs	$M_{Mn\text{-top}} = \pm 1, M_{Fe\text{-bottom}} = \pm 1$	130	520	$5 \times 5 \times 1$

4 Results and discussion

4.1 Structural statement

First, we optimized each monolayer to obtain the relaxed lattice parameters and atomic positions that serve as the structural baseline for the BL models. MSi_2N_4 ($\text{M} = \text{Fe}, \text{Mn}$) was relaxed in its hexagonal primitive unit cell (pcell) until the minimum-energy lattice constants and atomic coordinates were achieved. For Fe and Mn, the equilibrium in-plane lattice constants are $a = b = 2.8698$ Å and 2.847 Å, respectively. These calculations were performed without SOC. Our values are consistent with prior reports [68] and are summarized in Table 2.

The 2H- α phase examined in this work belongs to the D_{3h} point group (Schoenflies notation), or equivalently the nonsymmorphic $P\bar{6}m2$ space group (Hermann–Mauguin notation). This symmetry class contains a horizontal mirror plane (σ_h), three vertical mirror planes (σ_v), three twofold rotation axes (C_2), and a sixfold rotation axis (C_6), and is non-centrosymmetric. This symmetry class underlies several of the magnetic features discussed later. In particular, once SOC is included, MSN and FSN can break time-reversal symmetry and reduce the effective symmetry of the monolayers (MLs), a point we return to in the section on the primitive magnetic ground state.

Table 3 summarizes the optimized bond lengths. The transition-metal–nitrogen (TM–N) distances in the Fe, and Mn monolayers are 3.592/2.071, 3.495/1.995, and 3.483/1.989 Å, respectively.

To establish the structural configurations used later in our magnetic modeling, we considered all BL stackings compatible with the C_6 symmetry of these non-centrosymmetric MLs. In this work, the BLs correspond to MSN/FSN. Following the structural motifs explored in prior studies [69, 70], we examined three representative registry types. In the H3 (Hexagonal-3) arrangement [Fig. 1(a)], the

Table 2: Relaxed lattice constants, interlayer distance, magnetization, and MAE.

2D system	$a = b$ (Å)	d (Å)	M_{tot} (μ_B)	$M_{\text{TM}}/M_{(\text{TM-N})}$ (μ_B)	MAE (μRy)
FeSi ₂ N ₄	2.8698	—	3.61	—	49.2
MnSi ₂ N ₄	2.8470	—	3.199	—	−57.21
BL	2.851	3.108	8.17	3.02 / −0.192 3.50 / 0.026	$−1 \times 10^{-7}$

Table 3: Transition metal–inner nitrogen (TM–iN) I/II, silicon–inner nitrogen (Si–iN), and silicon–outer nitrogen (Si–oN) bonds.

2D system	TM-iN I (Å)	TM-iN II (Å)	Si-iN (Å)	Si-oN (Å)
FeSi ₂ N ₄	3.495	1.995	1.752	1.739
MnSi ₂ N ₄	3.483	1.989	1.751	1.735
BL				
MnSi ₂ N ₄	3.335	1.990	1.745	1.730
FeSi ₂ N ₄	3.473	1.984	1.746	1.730

transition metal (TM) atoms of one layer sit directly above the uppermost atomic plane of the adjacent layer. The T4 configuration [Fig. 1(b)] corresponds to a registry in which the top nitrogen atoms align across layers, a geometry that can also arise at grain boundaries due to local structural distortions [71]. A third configuration, labeled Top [Fig. 1(c)], places the surface nitrogen atoms in vertical alignment. Figure 1(d) provides a top view of these registries, emphasizing the interlayer atomic alignments.

All structures were fully relaxed in 1×1 BLs (with TM positions fixed) to allow for possible local reconstruction. We then scanned the interlayer separation ranging from ~ 10 Å down to the smallest non-bonding distance to map the potential energy surface (PES). In every case, its minimum corresponded to an H3-like stacking, as shown in Fig. 2, indicating that this registry is consistently the most stable non-covalently bonded configuration.

Additionally, strain can induce artificial proximity effects [72], potentially altering lattice constants, bond lengths, and even the resulting magnetic order. As shown in Table 2, however, the lattice constants of the BL differ by only $\sim 0.246\%$ from those of the isolated MLs. Such a small mismatch places the system well within the regime where strain-induced proximity effects can be safely neglected.

4.2 Primitive magnetic ground state

The magnetic properties of the constituent MLs play a central role in determining the ground-state behavior of the resulting vdWH. Because these layers exhibit distinct electronic and magnetic characteristics, it is necessary to examine how the interfacial environment in Bernal-like stackings modifies their interactions.

We first note that the net magnetizations of the MLs do not change abruptly under stacking, which supports our decision to neglect SOC in the Heisenberg modeling. This does not imply the absence of intrinsic SOC; rather, its contribution remains secondary to the dominant exchange processes. When SOC is included at the DFT level, the systems exhibit metallic behavior consistent with prior reports [45]. In this regime, Fe-containing MLs carry a larger magnetic moment ($3.61\mu_B$), indicating an increased density of spin-polarized conduction carriers (see Table 2).

Regarding the inquiry of how interlayer interactions modify the spin structure, we investigated it by examining the magnetic behavior of the BLs. As summarized in Table 4, the total energies of the various interlayer magnetic alignments all lie within ~ 3 meV of one another, indicating that the BL remains structurally stable regardless of the relative spin configuration [73]. Among these, the most energetically favorable ordering is $M_{B\uparrow}^{A\uparrow}$, followed sequentially by $M_{B\downarrow}^{A\uparrow}$ and $M_{B\uparrow}^{A\downarrow}$. The small energy differences between these states reveal a delicate balance of attractive and repulsive interlayer exchange channels, which in turn enable rapid vertical (interlayer) magnetic phase changes. The resulting

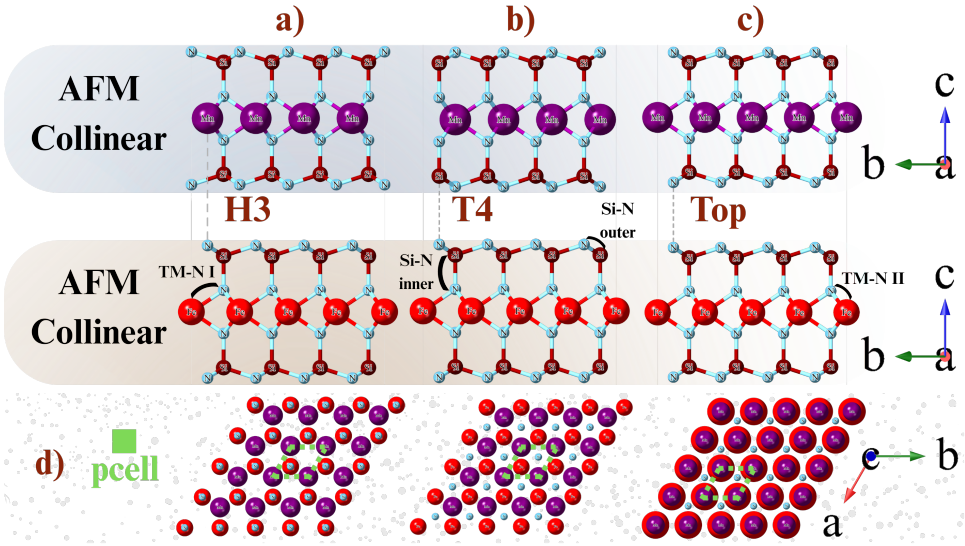


Figure 1: Side-view of the 2x2 BLs system showing the stacking a) H3, b) T4, c) Top where grey dashed lines point out high-symmetric interactions TM-N's. Structural sections d) display their top-view above, excluding silicones and non-interfacial nitrogens, separately. Pcells are labeled in green.

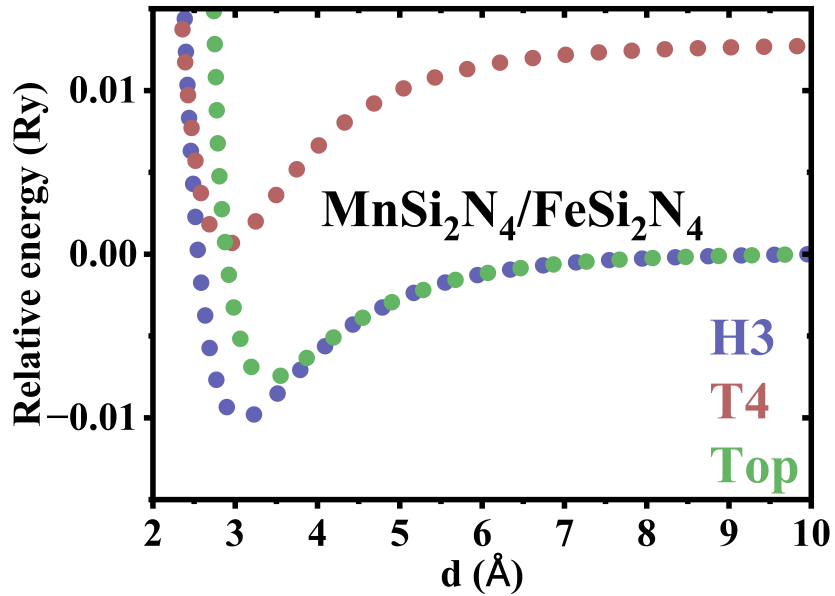


Figure 2: PES in the 1x1 BLs, where d is the interlayer distance.

Table 4: Relative energies for different magnetic alignments of the bilayer (BL). Energies are given relative to the lowest-energy configuration.

Configuration	$M_{(B\downarrow)}^{(A\uparrow)}$	$M_{(B\uparrow)}^{(A\downarrow)}$	$M_{(B\uparrow)}^{(A\uparrow)}$
Energy (mRy)	0.13	0.21	0
Layer	Mn (μ_B)	Fe (μ_B)	
BL	3.02	3.50	

interlayer coupling slightly reduces the local magnetic moments—by roughly $0.1 \mu_B$ —relative to the isolated monolayers.

Switchable magnetocrystalline anisotropy emerges in these magnetic compounds under charge doping, which perturbs the in-plane D_{3h} orbital environment. Although this mechanism does not induce the type of strongly mixed relativistic spinor structure generated by SOC in the (001) direction, it does break the in-plane symmetry and lifts the degeneracy between in-plane and out-of-plane spin orientations. Such symmetry lowering can also allow spin–quantum–Hall–like responses in principle.

To quantify the magnetic easy axis, we evaluate the Single-Ion Anisotropies (SIAs) extracted from the MAE calculations. FSN prefers an out-of-plane (OOP) easy axis, whereas MSN favors an in-plane (IP) alignment—consistent with the nearly isotropic crystal field experienced by Mn in this environment. The corresponding MAE values are $-669.401 \mu\text{eV}$ (-0.669 meV) for OOP alignment in FSN and $+778.382 \mu\text{eV}$ ($+0.778 \text{ meV}$) for IP alignment in MSN. These give SIA energies of $238.82 \mu\text{eV/Fe}$ and $-261.7 \mu\text{eV/Mn}$. The magnitude of the Mn SIA, particularly when compared with the reported $-365 \mu\text{eV/Mn}$ value, indicates that relativistic corrections and the exchange–correlation damping term play a significant role. It is well known that the Generalized Gradient Approximation tends to overestimate magnetic moments, while the Local Density Approximation underestimates exchange constants. Even so, our anisotropy values remain consistent with prior work and compare unfavorably against related Fe/Mn-based two-dimensional compounds. For example, Fe_3GeTe_2 monolayers exhibit an OOP MAE of 2.68 meV [74], substantially larger than our FSN result, it needs at least two single monolayers to conserve Weyl topological nodes [75] though. While the IP anisotropy and SIA reported for $\text{MnIn}_2\text{Se}_3\text{I}_2$ ($\sim 12.667 \text{ meV}$ and $931 \mu\text{eV}$) [76] are larger, but it arises in a far more structurally complex and defect-prone material. When on-site Coulomb interactions are incorporated through U_{eff} ,

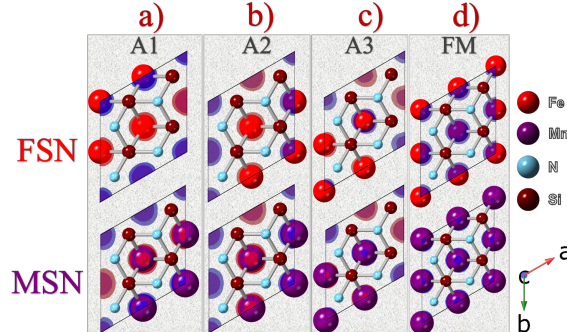


Figure 3: Spin isosurfaces for MSN and FSN in a 2×2 periodic arrangement. Blue and red lobes represent the accumulation of spin-up and spin-down probability densities, respectively, for each spin channel.

the MLs display AFM tendencies in accordance with Hund’s rules, consistent with earlier studies [66, 77]. Because the TM atoms occupy edge-sharing environments in our geometry, we reproduced the 2×2 magnetic configurations shown in Fig. 3 to verify the expected ordering. Although the magnetic moments differ slightly $-2.843 / -2.862 \mu_B$ for Mn and $\pm 3.318 \mu_B$ for Fe—this variation is consistent with a more accurate treatment of electronic correlations, including Becke–Johnson damping and tighter convergence thresholds [59]. Thus, our calculations remain in agreement with the predicted ML magnetic ground states while providing improved numerical precision.

Table 5: Relative energy, magnetic moments, and bond lengths for MSN and FSN under various magnetic configurations. Energies are relative to the ground state (A1).

System	Order	Rel. Energy (mRy)	μ_B per TM	Bonds (Å)		
				TM–N I	TM–N II	Si–iN/oN
MnSi ₂ N ₄	A1	0.000	+2.843, -2.862	3.476	1.984	1.747/1.732
	A2	9.567	+2.843, -2.862	3.476	1.984	1.745/1.729
	A3	9.571	+2.843, -2.862	3.467	1.983	1.745/1.729
	FM	83.277	± 2.831	3.471	1.987	1.745/1.729
FeSi ₂ N ₄	A1	0.000	± 3.436	3.482	1.980	1.744/1.735
	A2	1.107	± 3.436	3.480	1.979	1.745/1.734
	A3	1.107	± 3.436	3.473	1.980	1.745/1.735
	FM	27.882	± 3.318	3.478	1.984	1.746/1.733

On the other hand, when the Hubbard U and Hund’s coupling J are not included through Dudarev’s correction for the Fe- d and Mn- d orbitals in FSN and MSN [44], the MLs remain metallic in the spin-polarized channel. This contrasts with the primitive (i.e., $U \neq 0$) description, where the same systems appear half-metallic due to the effective Coulomb repulsion within the spinor manifold, which stabilizes sextet and octet spin multiplicities. A closer inspection of the separate roles of U and J further reveals that the coupling parameter J influences the Dirac-like valence band in MSN, modifying the relative splittings near the Fermi level.

In the AFM phases of MSN and FSN, the fully relaxed 2×2 supercells show that the Hubbard interaction changes the equilibrium volume (introducing local structural disorder)—consistent with previous studies [45, 46]. This indicates that the energetics of the AFM configurations depend sensitively on crystal-field splitting, whereas the FM phase remains comparatively unaffected, reflecting the presence of Kramers degeneracy and broken time-reversal symmetry only in the latter. As a result, the MLs adopt the magnetic space group $P_Bm\bar{n}2_1$ (type-IV), whose corresponding spin group is $P^1m^1m^{12-1}$. By symmetry, such a magnetic configuration cannot host an anomalous Hall effect.

4.2.1 Finite size in BLs All BL pcells were first relaxed while constraining the TM sites and allowing small displacements along the z -axis and in the (100)/(010) planes. This initial relaxation produced a modest surface reconstruction, characterized mainly by slight OOP shifts and small changes in local bond lengths. The reconstructed geometries were then used as input for building 2×2 supercells, which were again relaxed under the same TM constraints but with fixed IP lattice parameters and restricted OOP motion. These supercells provided the IP periodic boundary conditions employed in the magnetic calculations, which were performed self-consistently using the rotationally invariant Dudarev DFT+ U approach incorporating both Hubbard U and Hund J .

The Si–N sublayers in MA_2Z_4 play an essential structural and electronic role in stabilizing the magnetic BLs. Nitrogen contributes lone-pair p electrons that participate in mixed ionic–covalent bonding, forming a mechanically rigid and electronically active Si–N framework on either side of the TM plane. This bonding character allows charge redistribution across the BL without introducing strong covalency through the van der Waals gap, thereby maintaining well-defined local TM moments, as summarized in Table 6.

To fully characterize possible BL magnetic configurations, all symmetry-allowed combinations arising from the non-centrosymmetric MLs were examined. In total, eight distinct interlayer magnetic couplings were constructed and evaluated, consistent with the geometries illustrated in Fig. 6 of the Atomistic Exchange Model section.

Surface reconstruction effects, driven by the local changes in bond lengths, can be quantified directly from the DFT+ U results. Relative to the pcells, the AFM-coupled 2×2 BLs exhibit TM moment variations of approximately $+0.327/+0.308 \mu_B$ for Mn and $\pm 0.064 \mu_B$ for Fe. For FM-coupled BLs, the corresponding changes increase to $\pm 0.539 \mu_B$ and $\pm 0.285 \mu_B$, respectively. These magnetic reorganizations correlate with small but systematic modifications of the Si–iN and Si–oN bond lengths

in MSN (about -0.173% for FM and -0.400% for AFM), and similar changes for Mn-N(I/II) bonds (-0.197% for FM and -0.146% for AFM).

For FSN, the Si-iN/oN bond variations are -0.337% (FM) and -0.400% (AFM), while Fe-N(I/II) bonds shift by -0.197% (FM) and -0.823% (AFM). These distortions remain far from those required for a Jahn-Teller instability: the TM-N(I/II) octahedra do not distort toward a tetrahedral environment. However, the observed pattern of small bond-dependent moment changes suggests the possible emergence of nanoscale magnetic domain walls, similar to those recently identified in AFM BL materials such as CrSBr [78–81].

Table 6: Relationship of the various magnetic orders represented in Figure 6.

Order	Rel. Energy (mRy)	M_{Mn} (μ_B)	M_{Fe} (μ_B)	M_{Tot} (μ_B)	Distances (Å)		
					Mn-iN I/II	Fe-iN I/II	d
FM	63.64	3.17	3.60	28	2.030/2.030	2.050/3.512	2.915
A1	64.09	-3.17	3.60	-4.12	2.030/2.030	2.050/3.512	2.915
A2	64.13	3.17	-3.60	-4.12	2.030/2.030	2.050/3.512	2.92
C1	0.051	± 2.97	± 3.54	0	2.033/2.019	2.052/3.495	2.96
G1	0	± 2.97	± 3.54	0	2.033/2.019	2.052/3.495	2.96
C2	0	± 2.97	± 3.54	0	2.035/2.032	2.049/3.511	2.92
G2	0.782	± 2.97	± 3.54	0	2.035/2.032	2.049/3.511	2.92
C3	0.782	± 2.97	± 3.54	0	2.021/2.023	2.048/3.515	2.945
G3	0.884	± 2.97	± 3.54	0	2.021/2.023	2.048/3.515	2.945

4.3 Atomistic exchange model

To extract the effective exchange coupling constants, we adopt an isotropic Heisenberg description of the localized spin moments and neglect on-site magnetocrystalline anisotropy energy (MAE) [82]. The general form of the spin Hamiltonian is

$$\mathcal{H} = \sum_{i < j} \hat{\vec{S}}_i \cdot \mathbf{J}_{ij} \cdot \hat{\vec{S}}_j, \quad (1)$$

where \mathbf{J}_{ij} denotes the full exchange tensor coupling sites i and j [83, 84].

The MAE is omitted for two reasons. First, the energy differences used to extract J_a , J_d , and J_{2a} come from comparing collinear FM and AFM configurations; the MAE contributes only an overall shift and cancels exactly between these states. Second, the bilayer MAE obtained from DFT is extremely small (of order 10^{-7} μ Ry), meaning it does not influence the low-energy spectrum or the correlation observables obtained from exact diagonalization. In other words, the system is far from a spin-reorientation regime, and the isotropic Heisenberg form accurately captures the relevant physics [85].

We begin with the isolated monolayers (MLs), where the magnetic ions form nearly triangular in-plane arrays. Each ML is described using the three dominant intralayer exchange paths illustrated in Fig. 4: nearest neighbors (J_a), diagonal next-nearest neighbors (J_d), and second-nearest neighbors separated by twice the lattice constant (J_{2a}). This yields the single-layer effective model

$$\mathcal{H}_0 = J_a \sum_{\langle ij \rangle} \hat{\vec{S}}_i \cdot \hat{\vec{S}}_j + J_d \sum_{\langle\langle ij \rangle\rangle} \hat{\vec{S}}_i \cdot \hat{\vec{S}}_j + J_{2a} \sum_{\langle\langle\langle ij \rangle\rangle\rangle} \hat{\vec{S}}_i \cdot \hat{\vec{S}}_j, \quad (2)$$

where $J_{ij} < 0$ favors FM alignment and $J_{ij} > 0$ favors AFM alignment. The angled-bracket notation in the summation limits specifies the degree of nearness between lattice sites.

Using relaxation energies obtained from DFT for several magnetic configurations within a 2×2

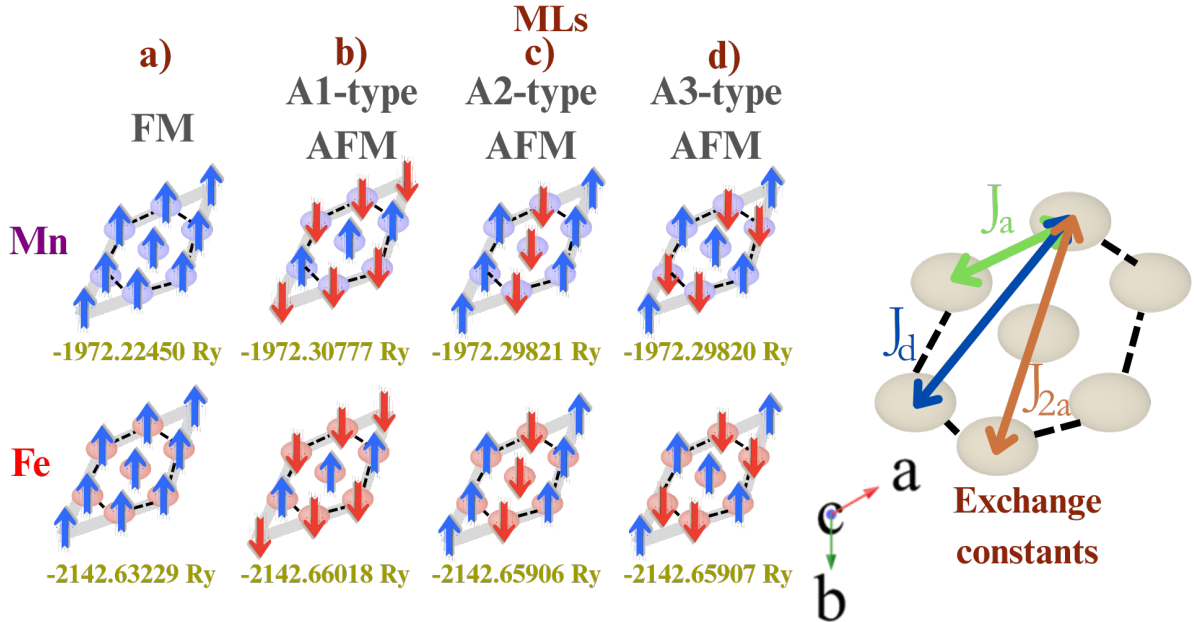


Figure 4: Representative model of nearest (J_a , exchange), next (J_d , double-exchange), and third (J_{2a} , super-exchange)-second-nearest neighbors intralayer terms for AFM/FM alignments: MSN and FSN in 2x2 periodicity.

periodic supercell (also shown in Fig. 4), we extract

$$\begin{aligned}
 E_F &= 2S_z^2(13J_a + 11J_d + 12J_{2a}), \\
 E_{A1} &= 2S_z^2(-5J_d + J_{2a}), \\
 E_{A2} &= 2S_z^2(-3J_a + 3J_d - 4J_{2a}), \\
 E_{A3} &= 2S_z^2(J_a - 5J_d + 3J_{2a}),
 \end{aligned} \tag{3}$$

with the corresponding energy differences

$$\begin{aligned}
 \Delta E_1 &= E_F - E_{A1} = 2S_z^2(13J_a + 16J_d + 11J_{2a}), \\
 \Delta E_2 &= E_F - E_{A2} = 16S_z^2(2J_a + J_d + 2J_{2a}), \\
 \Delta E_3 &= E_F - E_{A3} = 2S_z^2(12J_a + 16J_d + 9J_{2a}).
 \end{aligned} \tag{4}$$

For Mn ($S = 5/2$), this yields $J_a \approx -4.65$ meV (≈ -53.94 K), $J_d \approx +4.27$ meV ($\approx +49.54$ K), and $J_{2a} \approx +7.53$ meV ($\approx +87.35$ K). For Fe ($S = 7/2$), $J_a \approx +0.915$ meV ($\approx +10.61$ K), $J_d \approx +0.327$ meV ($\approx +3.79$ K), and $J_{2a} \approx -0.149$ meV (≈ -1.73 K). Even though Mn in MSN is a single monolayer of MA_2Z_4 , its intraexchange constant is much greater than that of bulk MnBi_2Te_4 of +0.4 meV [86] and +0.77 meV in undistorted MnPSe_3 [87]. This is one example of why the result is a breakthrough on its own. When comparing FSN exchanges with greater values in FM and AFM, favoring exchange values of 3.27 and -0.44 meV, respectively, in the bulk of Fe_3GeTe_2 [88], whose thickness is 8.6 Å, and its uncompensated $\text{Fe}^{2+}/\text{Fe}^{3+}$ itinerant ferromagnetic electrons, the result is significant. Similarly, FeCl_2 has a reported exchange constant of $J = +0.7$ meV at its Curie temperature $T_C = 13$ K [89]. At $T = 0$ K, this value is expected to be smaller, since DFT calculations include the dipole-dipole (zeroth-order) contribution that reduces the effective exchange.

4.3.1 Bilayer coupling We next couple the two MLs (Fig. 6) through interlayer Heisenberg exchange. Each site i in the top layer couples both to the vertically aligned site $j = i$ in the bottom layer (nearest interlayer neighbor) and to the surrounding sites sharing the same in-plane coordinate up to diagonal

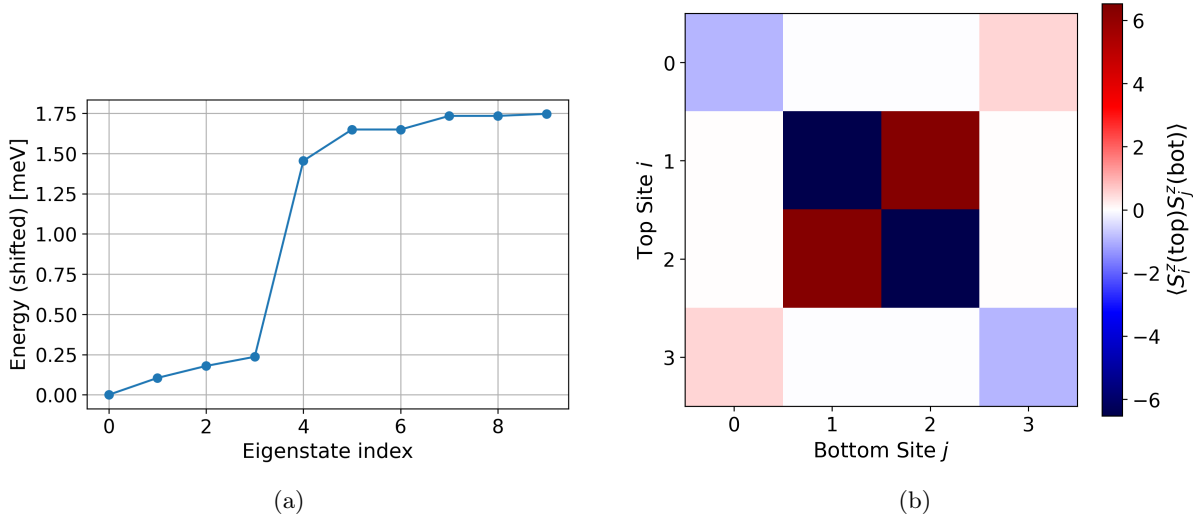


Figure 5: (a) Low-lying many-body spectrum of the $\text{MnSi}_2\text{N}_4/\text{FeSi}_2\text{N}_4$ bilayer Heisenberg model with toroidal boundary conditions, using intralayer and interlayer exchange parameters extracted from DFT. (b) Cross-layer spin–spin correlation matrix $\langle S_i^{z,\text{top}} S_j^{z,\text{bot}} \rangle_{\text{GS}}$. Red (blue) denotes ferromagnetic (antiferromagnetic) correlations between site i in the top layer and site j in the bottom layer. The alternating pattern among interior sites is consistent with the G2- and G3-type interlayer antiferromagnetic configurations shown in Fig. 6.

distance (next-nearest interlayer neighbors). The resulting bilayer Hamiltonian is

$$\mathcal{H} = \mathcal{H}_0 + \sum_{ij}^N J_{ij} \left(S_i^{z,\text{top}} S_j^{z,\text{bot}} + \frac{1}{2} (S_i^{+,\text{top}} S_j^{-,\text{bot}} + S_i^{-,\text{top}} S_j^{+,\text{bot}}) \right), \quad (5)$$

with N sites in each layer and the interlayer neighbor shells defined as $J_{\langle ij \rangle}$ (same site) and $J_{\langle\langle ij \rangle\rangle}$ (adjacent and diagonal sites).

Energy differences relative to the FM reference configuration yield

$$\begin{aligned} \Delta E_4 &= E_F - E_{A1} = 157.5 J_{\langle ij \rangle} + 218.75 J_{\langle\langle ij \rangle\rangle}, \\ \Delta E_5 &= E_F - E_{A2} = 350 J_{\langle\langle ij \rangle\rangle}. \end{aligned} \quad (6)$$

These give $J_{\langle ij \rangle} \approx +5.46$ meV (≈ 63.34 K) and $J_{\langle\langle ij \rangle\rangle} \approx -0.018$ meV (≈ -0.21 K).

Exact diagonalization of the bilayer Heisenberg Hamiltonian, Eq. 5, using the intralayer and interlayer exchanges extracted above, yields the low-lying spectrum shown in Fig. 5(a). The nondegenerate ground state in the $m = 0$ sector is separated from the first excited state by a gap of order 0.13 meV, while a group of higher excitations clusters between ~ 1.5 and 1.75 meV. To probe the real-space spin structure encoded in this ground state, we evaluate the cross-layer correlations $\langle S_i^{z,\text{top}} S_j^{z,\text{bot}} \rangle_{\text{GS}}$, shown in Fig. 5(b). White entries correspond to site pairs whose spin correlations vanish. This indicates that their contributions cancel across the quantum ground state superposition, either due to symmetry, frustration, or competing FM/AFM exchange paths. These pairs do not participate in the dominant interlayer ordering pattern. The alternating ferro- and antiferromagnetic correlations between the interior lattice sites reproduce the same ordering pattern as the G2- and G3-type interlayer antiferromagnetic configurations illustrated in Fig. 6. This establishes that the G-type arrangements dominate the low-energy spin texture of the $\text{MnSi}_2\text{N}_4/\text{FeSi}_2\text{N}_4$ bilayer and are the natural continuation of the monolayer-derived exchange interactions once the layers are coupled.

In summary, A1-type AFM for Mn and Fe MLs has the potential to modify the interaction in its entirety due to the finite size, given the existence of longer-range interactions. It has been demonstrated that both systems conserve $\hat{P}\hat{T}$ in the stripe AFM, thereby fostering the possibility of facile magnetic phase transitions (see reference [90, 91] for details). Magnetic transition from intralayer

MSN/FSN BLs

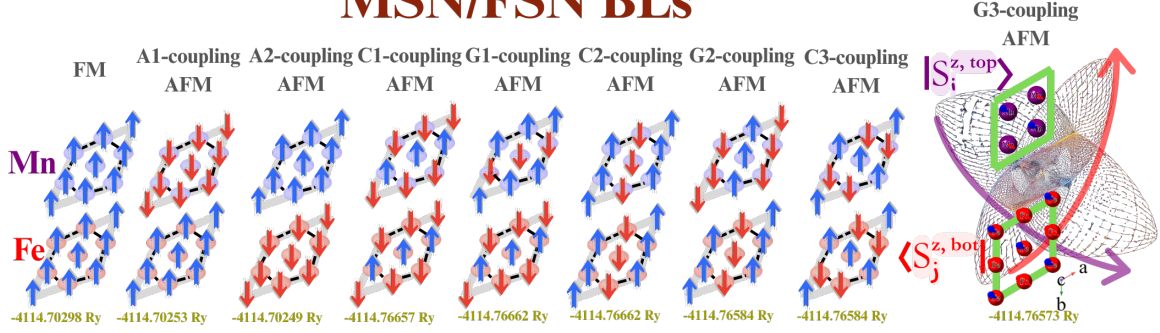


Figure 6: Representative model of FM, A-, C- and, G-couplings: $\text{MnSi}_2\text{N}_4/\text{FeSi}_2\text{N}_4$ – stacking H3 operated in the Heisenberg hamiltonian. It is worth noting that the BL allows four magnetic alignments more. A at G3-coupling

exchange A1-type in the isolated materials to A2-type and A3-type in the G2 and G3 couplings corroborates that a research gap remains concerning the absence of the necessity of SOC and how the conservation of flat bands and tilted cones in the pcells of A1-type MLs changes. This transformation of their ground state renders them not only superior to others but also exotic and non-trivial. Given the limitations imposed by the Mermin–Wagner theorem, the suppression of long-range antiferromagnetic order in the BL 2D regime leads to the formation of locally uncompensated spin regions. In the presence of external magnetic fields and proximity-induced itinerant carriers, these regions can act as effective internal exchange fields, leading to Zeeman-split electronic Landau levels. This scenario naturally points to the coexistence of two local spin multiplicities in the bilayer stacks, reflecting spatially inhomogeneous antiferromagnetic compensation.

5 Conclusions

In conclusion, the MA_2Z_4 bilayers studied here provide a compelling platform for exploring magnetic ordering and interlayer coupling in van der Waals systems. By combining first-principles calculations with an effective Heisenberg description and exact diagonalization, we demonstrate that the interlayer exchange interactions are non-perturbative and play a decisive role in shaping the magnetic ground state. Importantly, these interactions are comparable in magnitude to the dominant intralayer exchanges in at least one of the constituent layers, indicating that bilayer coupling cannot be treated as a weak correction to monolayer physics.

The robustness of the extracted exchange interactions across different supercell sizes and stacking configurations further indicates that the observed magnetic behavior is intrinsic to the bilayer geometry rather than a finite-size or symmetry artifact. While the present work focuses on static magnetic ordering and low-lying magnetic excitations, the resulting quantum correlation patterns highlight the importance of collective spin behavior beyond a purely single-particle picture.

These findings motivate future investigations into dynamical and transport phenomena in MA_2Z_4 heterostructures, where the interplay between strong exchange interactions, dimensionality, and symmetry may enable controllable spin configurations and antiferromagnetic functionality. In this context, a comprehensive understanding of spin dynamics should incorporate both localized magnetic excitations and collective spin-wave modes, particularly in regimes where antiferromagnetic correlations dominate.

Acknowledgements

The authors are grateful to Sergio E. Ulloa for insightful discussions on symmetry aspects of spin systems and the implications of spin–orbit coupling. The DFT calculations were carried out at the DGTIC-UNAM Supercomputing Center on the Xiuhtcoatl node as part of the LANCAD-CINVESTAV-CGSTIC-65-2026 project. The first author is grateful to the Nanoscale and Quantum Phenomena Institute (NQPI), Ohio University (OU), and Prof. Ulloa for the financial support in a research visit.

References

- [1] Liu L and Zhai T 2021 *InfoMat* **3** 3–21
- [2] Smejkal L, Sinova J and Jungwirth T 2025 *arXiv preprint arXiv:2508.09748* Submitted Aug 2025. Alternatively, check ACS Nano 2025 for 'Spintronic Devices upon 2D Magnetic Materials'
- [3] Jiang L N, Chi B Y and Han X F 2025 *Phys. Rev. B* **111**(22) 224422 URL <https://link.aps.org/doi/10.1103/39xc-2f3m>
- [4] Zhong H, Plummer D Z, Lu P, Li Y, Leger P A and Wu Y 2024 Integrating 2d magnets for quantum devices: from materials and characterization to future technology (*Preprint 2406.12136*) URL <https://arxiv.org/abs/2406.12136>
- [5] Zhang L, Yuan Z, Yang J, Zhou J, Jiang Y, Li H, Cai Y, Tsymbal E Y, Feng Y P, Zhu Z and Shen L 2024 *Phys. Rev. B* **110**(22) L220409 URL <https://link.aps.org/doi/10.1103/PhysRevB.110.L220409>
- [6] Sun Y, Meng F, Lee C, Soll A, Zhang H, Ramesh R, Yao J, Sofer Z and Orenstein J 2024 *Nature Physics* **20** 794–800
- [7] Qin P, Yan H, Wang X, Chen H, Meng Z, Dong J, Zhu M, Cai J, Feng Z, Zhou X, Liu L, Zhang T, Zeng Z, Zhang J, Jiang C and Liu Z 2023 *Nature* **613** 485–489
- [8] Chen X, Higo T, Tanaka K, Nomoto T, Tsai H, Idzuchi H, Shiga M, Sakamoto S, Ando R, Kosaki H, Matsuo T, Nishio-Hamane D, Arita R, Miwa S and Nakatsuji S 2023 *Nature* **613** 490–495
- [9] Selcuk K, Kanai S, Ota R, Ohno H, Fukami S and Camsari K Y 2024 *Phys. Rev. Appl.* **21**(5) 054002 URL <https://link.aps.org/doi/10.1103/PhysRevApplied.21.054002>
- [10] Němec P, Fiebig M, Kampfrath T and Kimel A V 2018 *Nature Physics* **14** 229–241
- [11] Sierra J F, Fabian J, Kawakami R K, Roche S and Valenzuela S O 2021 *Nature Nanotechnology* **16** 856–868
- [12] Wu S M, Zhang W, KC A, Borisov P, Pearson J E, Jiang J S, Lederman D, Hoffmann A and Bhattacharya A 2016 *Phys. Rev. Lett.* **116**(9) 097204 URL <https://link.aps.org/doi/10.1103/PhysRevLett.116.097204>
- [13] Dey P and Roy J N 2021 *Spintronics: Fundamentals and Applications* 1st ed (Springer Singapore) ISBN 978-981-16-0069-2 published: 13 April 2021
- [14] Wang X, Cao J, Lu Z, Cohen A, Kitadai H, Li T, Tan Q, Wilson M, Lui C H, Smirnov D, Sharifzadeh S and Ling X 2021 *Nature Materials* **20** 964–970
- [15] Kang S, Kim K, Kim B H, Kim J, Sim K I, Lee J U, Lee S, Park K, Yun S, Kim T, Nag A, Walters A, Garcia-Fernandez M, Li J, Chapon L, Zhou K J, Son Y W, Kim J H, Cheong H and Park J G 2020 *Nature* **583** 785–789
- [16] Jin Z, Meng C Y, Liu T T, Chen D Y, Fan Z, Zeng M, Lu X B, Gao X S, Qin M H and Liu J M 2021 *Phys. Rev. B* **104**(5) 054419 URL <https://link.aps.org/doi/10.1103/PhysRevB.104.054419>
- [17] He B, Jin H, Zheng D, Liu Y, Li J, Hu Y, Wang Y, Zhang J, Peng Y, Wan C, Zhu T, Han X, Zhang S and Yu G 2024 *Nano Letters* **24** 2196–2202
- [18] Telford E J, Dismukes A H, Lee K, Cheng M, Wieteska A, Bartholomew A K, Chen Y S, Xu X, Pasupathy A N, Zhu X, Dean C R and Roy X 2020 *Advanced Materials* **32** 2003240
- [19] Lee K, Dismukes A H, Telford E J, Wiscons R A, Wang J, Xu X, Nuckolls C, Dean C R, Roy X and Zhu X 2021 *Nano Letters* **21** 3511–3517

[20] Wilson N P, Lee K, Cenker J, Xie K, Dismukes A H, Telford E J, Fonseca J, Sivakumar S, Dean C, Cao T, Roy X, Xu X and Zhu X 2021 *Nature Materials* **20** 1657–1662

[21] Olsen T 2024 *2D Materials* **11** 033005 published online: 14 June 2024

[22] Chen H, Liu L, Zhou X, Meng Z, Wang X, Duan Z, Zhao G, Yan H, Qin P and Liu Z 2024 *Advanced Materials* **36** 2310379 (*Preprint*
<https://advanced.onlinelibrary.wiley.com/doi/pdf/10.1002/adma.202310379>) URL
<https://advanced.onlinelibrary.wiley.com/doi/abs/10.1002/adma.202310379>

[23] Lazić P, Sipahi G M, Kawakami R K and Žutić I 2014 *Phys. Rev. B* **90**(8) 085429 URL
<https://link.aps.org/doi/10.1103/PhysRevB.90.085429>

[24] Nair R R, Tsai I L, Sepioni M, Lehtinen O, Keinonen J, Krasheninnikov A V, Neto A H C, Katsnelson M I, Geim A K and Grigorieva I V 2013 *Nature Communications* **4** URL
<https://www.nature.com/articles/ncomms3010>

[25] Sverdlov V and Selberherr S 2015 *Physics Reports* **585** 1–40 ISSN 0370-1573 URL
<https://www.sciencedirect.com/science/article/pii/S0370157315002409>

[26] Kohn W and Sham L J 1965 *Physical Review* **140** A1133–A1138

[27] Dederichs P H, Blügel S, Zeller R and Akai H 1984 *Physical Review Letters* **53** 2512–2515

[28] Liechtenstein A I, Katsnelson M I, Antropov V P and Gubanov V A 1987 *Journal of Magnetism and Magnetic Materials* **67** 65–74

[29] Wang Q and et al 2021 *npj 2D Materials and Applications* **5**

[30] Ai H, Liu D, Geng J, Wang S, Lo K H and Pan H 2021 *Physical Chemistry Chemical Physics* **23** 3144–3151

[31] Wu Q and Ang L K 2022 *Applied Physics Letters* **120**

[32] Zhang Z, Wang J, Dai Z, Zhang M, Niu L and Bai L 2023 *Chemical Physics* **573** 111996

[33] Dey D, Ray A and Yu L 2022 *Physical Review Materials* **6**

[34] Zhang W, Yang W, Liu Y, Liu Z and Zhang F 2022 *Frontiers of Physics* **17**

[35] Liu C, Wang Z, Xiong W, Zhong H and Yuan S 2022 *Journal of Applied Physics* **131**

[36] Shu L, Qian L, Ye X and Xie Y 2022 *Physical Review Applied* **17** 054010

[37] Su X Q and Wang X F 2023 *Nanomaterials* **13** 676

[38] Zhang X, Liu B, Huang J, Cao X, Zhang Y and Guo Z X 2024 *Physical Review B* **109** 205105

[39] Ahmad S, Din H U, Nguyen C Q, Nguyen S T and Nguyen C 2024 *Dalton Transactions* **53** 3785–3796

[40] Yang C, Song Z, Sun X and Lu J 2021 *Physical Review B* **103** 035308

[41] Liang L, Yang Y, Wang X and Li X 2023 *Nano Letters* **23** 858–862

[42] Wang L and et al 2021 *Nature Communications* **12** 4–13

[43] Wang Z and et al 2022 *Applied Surface Science* **593** 153354

[44] Wu Q et al. 2022 *Applied Physics Letters* **120** 092406

[45] Zhao Z, Duan X, Fang X, Wang X and Mi W 2023 *Applied Surface Science* **611** 155693

[46] Tian M, Wei C, Zhang J and Wang Z 2022 *AIP Advances*

[47] Wei W, Xiang Y, Hou Q, Sun Y and Shi Z 2025 *Journal of Physics: Condensed Matter* **37** 143003 topical Review

[48] Chou C T, Ghosh S, McGoldrick B C, Nguyen T, Gurung G, Tsymbal E Y, Li M, Mkhoyan K A and Liu L 2024 *Nature Communications* **15**

[49] Šmejkal L, Jungwirth T, Sinova J and et al 2020 *Science Advances* **6** eaaz8809

[50] Mermin N D and Wagner H 1966 *Phys. Rev. Lett.* **17**(22) 1133–1136 URL <https://link.aps.org/doi/10.1103/PhysRevLett.17.1133>

[51] Park H, Kotliar G and Lee H 2025 *Physical Review B* **111**(15) 155122

[52] Giannozzi P *et al.* 2009 *J. Phys.: Condens. Matter* **21**

[53] Giannozzi P *et al.* 2020 *J. Chem. Phys.* **152**

[54] Blöchl P E 1994 *Phys. Rev. B* **50** 17953

[55] Joubert D 1999 *Phys. Rev. B* **59** 1758–1775

[56] Dudarev S L, Botton G A, Savrasov S Y, Humphreys C J and Sutton A P 1998 *Phys. Rev. B* **57** 1505

[57] Liechtenstein A I, Anisimov V I and Zaanen J 1995 *Phys. Rev. B* **52** R5467

[58] Grimme S, Antony J, Ehrlich S and Krieg H 2010 *J. Chem. Phys.* **132**

[59] Grimme S, Ehrlich S and Goerigk L 2011 *J. Comput. Chem.* **32** 1456–1465

[60] Perdew J P, Burke K and Ernzerhof M 1996 *Phys. Rev. Lett.* **77** 3865–3868

[61] Grimme S 2006 *J. Comput. Chem.* **27** 1787–1799

[62] Grimme S, Antony J, Ehrlich S and Krieg H 2010 *The Journal of Chemical Physics* **132** 154104 often cited for D3. For BJ-damping specifically, cite: J. Comput. Chem. 32, 1456 (2011)

[63] Becke A D and Johnson E R 2005 *The Journal of Chemical Physics* **123** 154101 ISSN 0021-9606 (Preprint https://pubs.aip.org/aip/jcp/article-pdf/doi/10.1063/1.2065267/13408810/154101_1_online.pdf) URL <https://doi.org/10.1063/1.2065267>

[64] Hubbard J 1963 *Proc. R. Soc. Lond. A* **276** 238–257

[65] Aikebaier F, Pertsova A and Canali C M 2015 *Phys. Rev. B* **92**

[66] An Z, Lv L, Su Y, Jiang Y and Guan Z 2023 *Physical Chemistry Chemical Physics* **26** 4208–4217

[67] Monkhorst H J and Pack J D 1976 *Phys. Rev. B* **13** 5188–5192

[68] Ren K, Shu H, Wang K and Qin H 2023 *Physical Chemistry Chemical Physics* **25** 4519–4527

[69] Pedroza-Rojas B, Sanchez-Castillo A and Ponce-Pérez R 2025 *ACS Omega* **10** 22062–22070 open Access, Published May 20, 2025 URL <https://pubs.acs.org/doi/10.1021/acsomega.5c02195>

[70] Bernal J D and Walker S J 1997 *Proceedings of the Royal Society of London. Series A, Containing Papers of a Mathematical and Physical Character* **1** 1123–1125

[71] Zande A M V D *et al.* 2013 *Nature Materials* **12** 554–561

[72] Žutić I, Matos-Abiague A, Scharf B, Dery H and Belashchenko K 2019 *Materials Today* **22** 85–107

[73] Tung R T and Kronik L 2016 *Physical Review B* **94** 1–24

[74] Jiang M C and Guo G Y 2022 *Phys. Rev. B* **105**(1) 014437 URL <https://link.aps.org/doi/10.1103/PhysRevB.105.014437>

[75] Roemer R, Lee D H D, Smit S, Zhang X, Godin S, Hamza V, Jian T, Larkin J, Shin H, Liu C, Michiardi M, Levy G, Zhang Z, Green R J, Kim C, Muller D, Damascelli A, Han M J and Zou K 2024 *npj 2D Materials and Applications* **8** 63 ISSN 2397-7132 URL <https://doi.org/10.1038/s41699-024-00499-0>

[76] Yang Y, Chen X, Zhang G, Li K, Wang J and Chen Q 2025 *Phys. Rev. B* **112**(18) 184426 URL <https://link.aps.org/doi/10.1103/hnm7-xz31>

[77] Chen D *et al.* 2022 *Frontiers in Chemistry* 1–7

[78] Hedrich N, Wagner K, Pylypovskiy O V, Shields B J, Kosub T, Sheka D D, Makarov D and Maletinsky P 2021 *Nature Physics* **17** 574–577 ISSN 1745-2481 URL <https://doi.org/10.1038/s41567-020-01157-0>

[79] Zur Y, Noah A, Boix-Constant C, Mañas-Valero S, Fridman N, Rama-Eiroa R, Huber M E, Santos E J G, Coronado E and Anahory Y 2023 *Advanced Materials* **36** 2307195 URL <https://doi.org/10.1002/adma.202307195>

[80] Tschudin M A, Broadway D A, Siegwolf P, Schrader C, Telford E J, Gross B, Cox J, Dubois A E E, Chica D G, Rama-Eiroa R, J G Santos E, Poggio M, Ziebel M E, Dean C R, Roy X and Maletinsky P 2024 *Nature Communications* **15** 6005 ISSN 2041-1723 URL <https://doi.org/10.1038/s41467-024-49717-9>

[81] Sun Z, Hong C, Chen Y, Sheng Z, Wu S, Wang Z, Liang B, Liu W T, Yuan Z, Wu Y, Mi Q, Liu Z, Shen J and Wu S 2025 *Nature Materials* **24** 226–233 ISSN 1476-4660 URL <https://doi.org/10.1038/s41563-024-02074-w>

[82] Choi D J, Lorente N, Wiebe J, von Bergmann K, Otte A F and Heinrich A J 2019 *Rev. Mod. Phys.* **91**(4) 041001 URL <https://link.aps.org/doi/10.1103/RevModPhys.91.041001>

[83] Facemyer D W, Dandu N K, Lee A T, Singh V R, Ngo A T and Ulloa S E 2023 *Phys. Rev. B* **108**(8) 085407 URL <https://link.aps.org/doi/10.1103/PhysRevB.108.085407>

[84] Facemyer D W and Ulloa S E 2025 *Phys. Rev. B* **111**(6) 064403 URL <https://link.aps.org/doi/10.1103/PhysRevB.111.064403>

[85] Xiang H J, Lee C, Koo H J, Gong X G and Whangbo M H 2013 *Dalton Trans.* **42** 823–853

[86] Chen B, Liu X, Li Y, Tay H, Taniguchi T, Watanabe K, Chan M H W, Yan J, Song F, Cheng R and Chang C Z 2024 *Nano Lett.* **24** 8222–8229

[87] Calder S, Haglund A V, Kolesnikov A I and Mandrus D 2021 *Phys. Rev. B* **103**(2) 024414 URL <https://link.aps.org/doi/10.1103/PhysRevB.103.024414>

[88] Liu Q, Xing J, Jiang Z, Guo Y, Jiang X, Qi Y and Zhao J 2022 *Communications Physics* **5** 140 ISSN 2399-3650 URL <https://doi.org/10.1038/s42005-022-00921-3>

[89] Yang Y, Guo P and Luo Y 2020 *Physical Chemistry Chemical Physics* **22** 17291–17298 ISSN 1463-9076 published 03 Jul 2020 URL <https://doi.org/10.1039/D0CP01422B>

[90] Šmejkal L, González-Hernández R, Jungwirth T and Sinova J 2020 *Science Advances* **6** eaaz8809 (*Preprint* <https://www.science.org/doi/pdf/10.1126/sciadv.aaz8809>) URL <https://www.science.org/doi/abs/10.1126/sciadv.aaz8809>

[91] Zhou P, Peng X N, Hu Y Z, Pan B R, Liu S M, Lyu P and Sun L Z 2025 *Physical Review B* **112** 144419 last revised 15 Oct 2025 (v3) (*Preprint* [arXiv:2410.17747](https://arxiv.org/abs/2410.17747)) URL <https://arxiv.org/abs/2410.17747>